ORIGINAL PAPER

A hybrid experimental/numerical technique to extract cohesive fracture properties for mode-I fracture of quasi-brittle materials

Arun L. Gain · Jay Carroll · Glaucio H. Paulino · John Lambros

Abstract We propose a hybrid technique to extract cohesive fracture properties of a quasi-brittle (not exhibiting bulk plasticity) material using an inverse numerical analysis and experimentation based on the optical technique of digital image correlation (DIC). Two options for the inverse analysis were used—a shape optimization approach, and a parameter optimization for a potential-based cohesive constitutive model, the so-called PPR (Park-Paulino-Roesler) model. The unconstrained, derivative free Nelder-Mead algorithm was used for optimization in the inverse analysis. The two proposed schemes were verified for realistic cases of varying initial guesses, and different synthetic and noisy displacement field data. As proof of concept, both schemes were applied to a Polymethyl-methacrylate (PMMA) quasi-static crack growth experiment where the near tip displacement field was obtained experimentally by DIC and was used as input to the optimization schemes. The technique was successful in predicting the applied load-displacement response of a four point bend edge cracked fracture specimen.

A. L. Gain · G. H. Paulino (✉)
Department of Civil and Environmental Engineering,
University of Illinois at Urbana-Champaign,
205 N. Mathews Ave., Urbana, IL 61801, USA
e-mail: paulino@illinois.edu

J. Carroll
Department of Mechanical Science and Environmental
Engineering, University of Illinois at Urbana-Champaign,
1206 W. Green St., Urbana, IL 61801, USA

J. Lambros
Department of Aerospace Engineering, University of Illinois at
Urbana-Champaign, 104 S. Wright St., Urbana, IL 61801, USA

1 Introduction

Cohesive zone modeling (CZM) has been extensively used in the past in problems dealing with debonding, delamination, crack propagation/initiation, etc. Barenblatt (1959) used the concept of CZM wherein fracture in perfectly brittle materials can be modeled as material separation across a surface. Later Dugdale (1960) extended the concept to perfectly plastic materials by suggesting the existence of plastic zone at the crack tip. Hillerborg et al. (1976), based on the ideas of Dugdale and Barenblatt, proposed the fictitious crack model for analyzing crack growth in concrete, since then a very popular model in civil engineering applications. Other researchers such as Needleman (1987) came up with exponential and polynomial type CZMs which were used to simulate particle debonding in metal matrices. Xu and Needleman (1993) later used the above models to study void nucleation at an interface between a particle and matrix. Ritchie et al. (1997) studied the behavior of cracks near a thin metallic layer joining monolithic ceramic substrates.

Although early Dugdale-Barenblatt type models involved a surface with a constant traction-separation relation, as has been seen through the efforts of many researchers since, the shape of the specific traction-separation relation in a CZM plays an important role in its behavior in a simulation framework. For instance, Volokh (2004) compared bilinear, parabolic, sinusoidal and exponential CZMs using a block-peel test. Using a block-peel test, they show that contrary to popular belief that cohesive strength and fracture energy are the sole important factors in a CZM, the shape of the CZM significantly affects the results. A similar study was performed by Alfano (2006) who utilized mode-I and mode-II simulations to pinpoint the differences arising because of the use of different traction-separation relations such as bilinear, linear-parabolic, exponential, and trapezoidal. They concluded that the effect of the shape of the CZM on numerical results depends on the boundary conditions of the problem and the ratios of the interface toughness and the stiffness of the bulk material. Chandra et al. (2002) performed a detailed investigation of fracture processes in a number of material systems utilizing many well known CZMs and showed that the shape of the CZM plays a critical role in determining the macroscopic response of a composite system. Song et al. (2008) analyzed the influence of the shape of CZMs on asphalt concrete fracture. Gu (1995) showed that, under large scale bridging, the shape of the cohesive zone model influences the load carrying capacity of a plate with an elliptical hole. Different crack bridging mechanisms, modeled using micromechanical models, also result in cohesive models with varied shapes. For instance, Budiansky et al. (1995) have shown that for the case when crack bridging is done using weakly bonded, frictionally restrained long fibers oriented perpendicular to the crack plane, the cohesive stress increases proportionally to the square root of the crack opening displacement. Spearing and Evans (1992) have shown that fibers oriented parallel to the crack plane produces a cohesive model in which cohesive stress decreases with an increase in crack opening displacement.

It is clear, therefore, that the shape, and of course values, of the traction-separation relations employed are instrumental in the model's usefulness. Thus, as with many such failure theories that are externally imposed from a simulation framework, how one goes about extracting or developing a traction-separation relation is a critical link in the methodology. There are several

ways in which one can obtain a cohesive zone model, chief among them being some calibration with, or prediction from, experiments. Direct tension tests have been utilized in the past by some researchers (van Mier and van Vliet (2001)) for this purpose, although a direct connection from a macroscale experiment to a local characteristic such as the CZM is not straightforward. Another approach is to directly measure traction-separation relations from some type of local or multiscale experimentation (e.g., Abanto-Bueno and Lambros 2005). Kaute et al. (1993) directly obtained the relationship between bridging stress and crack opening for delamination cracking in unidirectional SiC-fiber reinforced calcium aluminosilicate (CAS-SiC). Using the concept of J integral Sorensen and Jacobsen (1998), experimentally measured the bridging law for a double cantilever beam specimen, composed of a unidirectional carbon fiber epoxy composite, with pure bending moments applied. Andersson and Stigh (2004) determined the stress-elongation relation for a thin epoxy adhesive loaded in peel by using equilibrium of energetic forces. There are also some indirect approaches that have been proposed in the recent past that generally involve less difficult experimentation procedures. Kandula et al. (2006) performed an indirect approach of calibrating static CZM based fracture simulations with locally measured failure quantities from independent uniaxial tension experiments. Results of macroscale force-displacement measurements in fracture experiments were then used as a basis for successful calibration of the CZM and separate experiments were used to validate the model. Elices (2002) have also documented a number of such indirect methods. A common characteristic in all these indirect methods is that they all use global responses, such as load versus crack mouth opening displacement, as an input to some sort of inverse analysis which then provides the traction versus separation relation characteristic of the fracture of the specimen material.

Recent developments in the field of optical devices and image processing techniques have facilitated measurement of full-field displacement fields. These displacement fields combined with suitable inverse computational technique have been used to identify mechanical properties of materials. Avril et al. (2008) have conducted a detailed study of inverse computation techniques based on full-field measurements. The finite element model updating (FEMU) method (Cottin et al. 1984; Pagnacco et al. 2005) is one of the pop-

ular inverse technique of choice. FEMU minimizes the variations between either known and predefined forces (FEMU-F), or known and predicted displacement fields (FEMU-U). The constitutive equation gap method is another scheme which is based on minimizing the difference between a given stress field and the stress field computed using an assumed constitutive model along with a given displacement field (Ladevèze et al. 1994). An approach named as the virtual field method, based on the virtual work principle, has emerged more recently (Grédiac and Pierron 2006). It is used to identify the mechanical properties of materials for which strain fields are known experimentally. The equilibrium gap method is an inverse analysis scheme used to determine heterogeneous elastic fields by minimizing the equilibrium gap (Claire et al. 2004). An inverse scheme termed the reciprocity gap method, based on the Maxwell-Betti reciprocity theorem and adjoint fields, is used in situations where mechanical field measurements are available on the boundaries. Mechanical properties are found by minimizing the reciprocity gap for any adjoint field (Calderon 1980).

Nonetheless, none of these methodologies have been in any way standardized, and much needs to be done to improve ways of evaluating CZM properties. This paper investigates a hybrid (numerical/experimental) technique which makes use of both inverse numerical simulations and optical experimental technique of Digital Image Correlation (DIC), making the use of global load-deflection response an independent validation rather than a means of obtaining CZM properties. The Nelder-Mead (N-M) scheme which is an unconstrained, derivative free optimization scheme, is used for the inverse analysis. Physical constraints such as positive traction along crack faces for mode-I fracture are imposed using barrier functions. Two options for the inverse analysis are adopted: namely, a shape optimization approach, and a parameter optimization for the PPR (Park-Paulino-Roesler) potential-based CZM. In the shape optimization approach, we optimize the location of points in the traction-separation domain which are later interpolated to obtain the inherent cohesive zone model. In the parameter optimization for the PPR potential-based CZM, we optimize the PPR parameters of cohesive strength, fracture energy and shape parameter. Both the proposed schemes are verified for various plausible cases. The goal of the paper is also to validate the hybrid scheme using PMMA quasi-static crack growth experiment. Inverse analysis takes the

local displacement fields coming from the DIC procedure for PMMA as input and validates the result against the global sample response. Recently, Shen and Paulino (2010a) proposed a similar technique to extract CZM associated with material fracture for an elastic bulk material using combination of inverse analysis and digital image correlation. They used a shape optimization technique for the CZM, in which the FEMU-U approach was used for the inverse analysis and applied it to compute the cohesive properties of a ductile adhesive, Devcon Plastic Welder II (with PMMA as the bulk material), and G-10/FR4 Garolite. We have adopted the FEMU-F approach for our inverse analysis schemes. The modifications here are that in addition to a shape optimization approach, we also use a parameter optimization for the PPR (Park-Paulino-Roesler) potential-based CZM which has not appeared in literature before. Our validation experiment is aimed at estimating the cohesive fracture properties of PMMA (single specimen without any adhesive bonding).

The remainder of the paper is organized as follows: Section 2 presents the two proposed inverse analysis approaches. Both direct and inverse problems are discussed for the two schemes. Section 3 shows two demonstrative examples, one for each approach. We verified both schemes for various initial guesses, different displacement field data and noisy displacement field data. Section 4 demonstrates the use of the proposed concepts by applying the hybrid scheme to a PMMA quasi-static crack growth four point bending edge crack experiment.

2 Shape optimization approach

The underlying concept in the shape optimization technique is that the material specific CZM is obtained from interpolation of points on the traction-separation domain. The locations of points are determined using the Nelder-Mead optimization technique.

2.1 Direct problem

Formulation of the direct problem is based on the principle of virtual work. The sum of internal work done by the virtual strain $\delta\boldsymbol{\varepsilon}$ in the domain Ω and internal work done by the virtual crack opening displacement $\delta\boldsymbol{d}$ along the crack line Γ_c is equal to the external

work done by virtual displacement $\delta\boldsymbol{u}$ along the traction boundary Γ. Moreover, $\mathbf{T}_c$ is the cohesive traction generated on the surface of the crack due to applied virtual displacement $\delta\boldsymbol{u}$, and $\mathbf{T}_{ext}$ is the externally applied traction. Thus, the weak form is expressed as

$$\int_\Omega \delta\boldsymbol{\varepsilon}^T \cdot \boldsymbol{\sigma}\, d\Omega + \int_{\Gamma_c} \delta\boldsymbol{d}^T \cdot \boldsymbol{T}_c d\Gamma_c = \int_\Gamma \delta\boldsymbol{u}^T \cdot \boldsymbol{T}_{ext}\, d\Gamma \tag{1}$$

Using shape function derivative matrix $\boldsymbol{B}$ and shape function matrix $\boldsymbol{N}$, Eq. (1) can be rewritten as follows (Park et al. 2009; Song 2006),

$$\left(\int_\Omega \boldsymbol{B}^T \mathbf{E}\boldsymbol{B}\, d\Omega + \int_{\Gamma_c} \boldsymbol{N}^T \frac{\partial \boldsymbol{T}_c}{\delta\boldsymbol{d}} N\, d\Gamma_c \right) \boldsymbol{u} = \int_\Gamma \mathbf{T}_{ext}\, d\Gamma \tag{2}$$

$$(\mathbf{K}_b + \mathbf{K}_{coh}(\boldsymbol{u}, \boldsymbol{\lambda}_{coh}))\,\boldsymbol{u} = \mathbf{F}^{ext} \tag{3}$$

where, $\mathbf{E}$ is the material tangent matrix, $\boldsymbol{\lambda}_{coh}$ is the set of cohesive parameters which defines the cohesive zone model, and $\mathbf{K}_b$, $\mathbf{K}_{coh}$, and $\mathbf{F}^{ext}$ are given as

$$\mathbf{K}_b = \int_\Omega \boldsymbol{B}^T \mathbf{E}\boldsymbol{B}\, d\Omega, \qquad \mathbf{K}_{coh} = \int_{\Gamma_c} \boldsymbol{N}^T \frac{\partial \mathbf{T}_c}{\delta\boldsymbol{d}} N\, d\Gamma_c,$$

$$\mathbf{F}^{ext} = \int_\Gamma \mathbf{T}_{ext}\, d\Gamma \tag{4}$$

In the direct problem, the material properties (e.g., Young's modulus, Poisson's ratio and associated CZM) are known a priori. Simulation output is obtained in the form of load versus crack mouth displacement (CMOD) or load versus load line displacement (LLD), etc. At each loading step, the entire displacement field of the specimen is also obtained. The Newton-Raphson scheme is used to solve this nonlinear problem. Current work concentrates on the two dimensional case with mode-I symmetry. Consider a two dimensional specimen as shown in the Fig. 1. The specimen is simply supported and loaded in four point bending such that the crack propagates along the line of symmetry. Taking advantage of symmetry, only half of the beam is considered. Cohesive line elements are inserted directly ahead of the starter crack along the line represented by the thick line in Fig. 1.

2.2 Inverse problem

The inverse problem is governed by the same equation as the direct problem (Eq. (3)) with the only difference
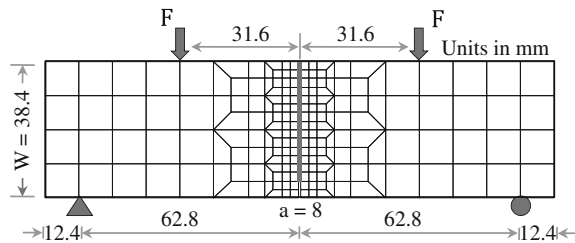

Fig. 1 Specimen geometry for the numerical examples. The initial crack length is denoted by 'a'

that now the displacement field $\boldsymbol{u}$ would be considered known (either, for example, from the direct problem simulation or from independent experimentation) and the unknowns are the cohesive parameters $\boldsymbol{\lambda}_{coh}$ which represent the unknown coordinates of a number of points on the traction-separation curve as shown in Fig. 2, i.e. $\boldsymbol{\lambda}_{coh} = \{X_1, X_2, \ldots, X_n, Y_1, Y_2, \ldots, Y_n\}$

The cohesive parameters are estimated using an optimization scheme which minimizes the following function including norm of the residual and barrier functions,

$$\min_{\boldsymbol{\lambda}_{coh}} \Phi(\lambda_{coh}) = w_1 ||\mathbf{F}^{ext} - \mathbf{F}^{int}||$$
$$+ w_{f1} f_1(\mathbf{Y}) + w_{f2} f_2(\mathbf{X}), \qquad \Phi : \mathbb{R}^{2n} \to \mathbb{R} \tag{5}$$

where, $\mathbf{F}^{int} = (\mathbf{K}_b + \mathbf{K}_{coh}(\boldsymbol{u}, \boldsymbol{\lambda}_{coh}))\,\boldsymbol{u}$; 2n represents the number of cohesive parameters being optimized; w_1, w_{f1}, w_{f2} are the weighting factors; $\mathbf{X} = \{X_1, X_2, \ldots X_n\}$; $\mathbf{Y} = \{Y_1, Y_2, \ldots Y_n\}$. The inherent CZM is obtained by interpolating the optimized points. Piecewise Cubic Hermite (PCH) interpolation has been used in this study. The optimization scheme is terminated when the change in objective function is less than 0.1 percent. This technique is capable of producing
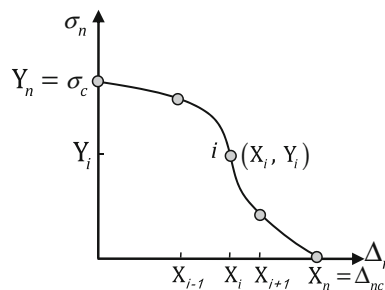

Fig. 2 Illustration of cohesive parameters for shape optimization approach. The circles represent the interpolation points whose coordinates are being optimized. CZM is obtained by interpolation of these points

CZMs of any shape regardless of the how complicated it might be because the shape is not assumed beforehand but rather comes out of an optimization, which is rarely seen in literature (Shen 2009; Shen et al. 2010b). At this stage, for technique development purposes, the inverse problem takes the displacement fields resulting from the direct problem as input. Note that, as will be subsequently, the displacement field corresponding to any single value of applied load in the direct problem can be chosen for the inverse analysis provided that the complete cohesive zone has been fully formed at this load.

Optimization is carried out using the Nelder-Mead (N-M) optimization scheme (Nelder and Mead 1965). The N-M algorithm belongs to the class of direct search algorithms. It uses a series of simplexes (entities which depend on the number of unknowns in the optimization problem e.g., line for single unknown, triangle for two unknowns, tetrahedron for three unknowns etc.) to minimize a scalar function of variables using the function value only. The distinguishing feature of the N-M scheme is that it is an unconstrained optimization (i.e., the variable being optimized $x \in (-\infty, \infty)$). It is derivative free, so there is no need to calculate the Jacobian or Hessian (thus avoiding a lot of potential numerical errors). A flow chart illustrating the N-M scheme is shown in Fig. 3. For algorithm details see Nelder and Mead (1965).

The N-M scheme is an unconstrained optimization so the cohesive parameters are allowed to take any value $\in (-\infty, \infty)$. However, physically it makes no sense for the cohesive parameters to take any value e.g. the tractions for mode-I fracture can only be tensile in nature i.e. $\sigma > 0$, for mode-I fracture. Also $X_1 < X_2 < \cdots < X_{i-1} < X_i < X_{i+1} < \cdots < X_n$ would have to be enforced to ensure no snap back behavior (i.e., $X_{i-1} > X_i$). These constraints are incorporated into the N-M optimization through the use of barrier functions f_1, f_2 given by,

$$f_1(\mathbf{Y}) = \sum_i 10^{\Psi_1(\gamma_1 - \gamma_i)}, \quad f_2(\mathbf{X}) = \sum_i 10^{\Psi_2(\zeta_i - \gamma_2)} \quad (6)$$

where, $\gamma_i << 1$, $\Psi_i >> 1$, also

$$\zeta_i = \left| \frac{X_i - \frac{X_{i+1}+X_{i-1}}{2}}{\frac{X_{i+1}-X_{i-1}}{2}} \right| \quad (7)$$

The barrier function assumes a negligible value when in the feasible region but reaches a very high value when the forbidden region is approached. In the literature, various barrier functions have been used such as inverse barrier functions, logarithmic functions and exponential barrier functions (Nocedal and Wright 2006). As seen in Eq. 6, exponential type barrier functions have been chosen for the current analysis.

The inverse analysis is known to be ill-posed with no unique solution. In order to prevent the algorithm from getting bogged down at one of the local minima, regularization needs to be performed. Through regularizations we ensure that non-physical CZMs are removed if and when they arise during optimization. The regularization schemes similar to one used by Shen (2009), Shen et al. (2010b) have been used. Our first regularization scheme ensures that the points being optimized are certain predefined distance apart, preventing them from forming a cluster. The cluster needs to be avoided to facilitate convergence. Clusters are removed as follow. Consider that we have n points $(P_1, P_2, \ldots, P_i, \ldots, P_n)$ on the traction-separation curve whose locations $(\{X_1, Y_1\}, \{X_2, Y_2\}, \ldots, \{X_i, Y_i\}, \ldots, \{X_n, Y_n\})$ we are trying to optimize. First we calculate the distance between adjacent points on the traction-separation curve. Let the distances be $(d_1, d_2, \ldots, d_i, \ldots, d_{n-1})$ and the maximum distance be d_{max}. Suppose $d_i < \alpha d_{max}$ (α is chosen by the user, we used $\alpha = 1/6$), which means points P_i and P_{i+1} are too close to each other. So point P_{i+1} is removed and in its place, a point P_k is added to the CZM such that $X_k = (X_i + X_{i+2})/2$ and Y_k is the value of traction at X_k on the previously converged CZM. Other scheme we used removed any non physical CZM (such as highly fluctuating CZM) that emerged during any iteration. The fluctuations in CZM are removed as follows: Consider the case when the points P_{i-1}, P_i, P_{i+1} are located close to each other such that $(X_{i-1} - X_i) \approx (X_i - X_{i+1}) \approx \beta X_{max}$ (β is chosen by the user, we used $\beta = 1/20$) and $Y_i >> Y_{i-1}, Y_i >> Y_{i+1}$. Clearly the point P_i causes instability and needs to be removed. So the points P_i and P_{i+1} are removed and in their place two points are added to the CZM in a way similar to the cluster case discussed above. Both the above schemes are conducted automatically after each iteration without any outside intervention. Although these regularization schemes are heuristic in nature, along with the barrier functions they have proven sufficient to stabilize the algorithm.
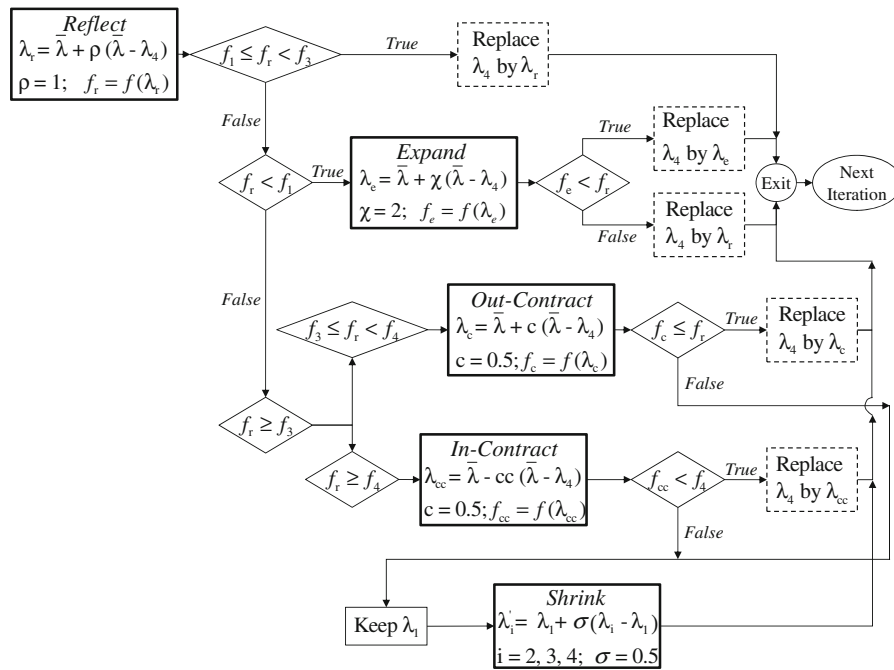
Fig. 3 Flow chart illustrating Nelder-Mead optimization scheme for three unknowns. $\lambda_i's$, $i = 1 - 4$, are the points in the space defined by the three unknowns with corresponding objective function values $f_i's$. For three unknowns, the simplex is a tetrahedron. λ_r, λ_e, λ_c, and λ_{cc} are the reflection, expansion, outside-contraction, and inside-contraction points respectively. Assuming we have a minimization problem and $f_1 < f_2 <$

$f_3 < f_4$, the objective for each iteration is to replace the worst λ_i (which is λ_4 is this case) with a better approximation (λ_r, λ_e, λ_c, or λ_{cc}). ($\bar{\lambda}$ is the centroid of the triangle formed by λ_1, λ_2, and λ_3. At the end of each iteration, if none of the conditions for f_r, f_e, f_c, or f_{cc} are satisfied then λ_1 is retained (best point) and rest of the three vertices are obtained by shrinking the tetrahedron

3 Parameter optimization for the PPR potential-based CZM

The Park-Paulino-Roesler model (Park et al. 2009) was chosen for this work because it provides a single closed potential function which can be used to obtain traction-separation curves for both mode-I and II and can provide both intrinsic and extrinsic CZMs. For the mixed mode case, different fracture energies and cohesive strengths can be specified. Just by determining few parameters (the fracture energy, cohesive strength, and shape parameter in an extrinsic mode-I case; and additionally the initial slope for the intrinsic case) the CZM can be uniquely defined. Although we only deal with mode-I here, the PPR provides a platform for our work to be extended to mixed mode fracture.

3.1 Direct problem

The formulation for the direct problem is the same as the previously proposed scheme (Eqs. (1)–(4)). The

CZM comes from the derivative of the PPR potential. For the mode-I extrinsic model, the normal traction versus normal separation relation is given by Eq. (8). Knowing the parameters: fracture energy ϕ_n, cohesive strength σ_c, and shape parameter α, the CZM can be uniquely defined.

$$\sigma_n(\Delta_n) = \alpha \frac{\phi_n}{\delta_n} \left(1 - \frac{\Delta_n}{\delta_n} \right)^{\alpha - 1} \tag{8}$$

where, α_n is the normal traction, Δ_n is the normal crack separation, and δ_n are given by

$$\delta_n = \frac{\alpha \phi_n}{\sigma_c} \tag{9}$$

3.2 Inverse problem

The objective in this approach is to optimize the cohesive parameters $\lambda_{coh} = \{\phi_n, \sigma_c, \alpha\}$ using the Nelder-Mead optimization scheme. The reason why PPR is attractive for inverse analysis is that it is a unified model
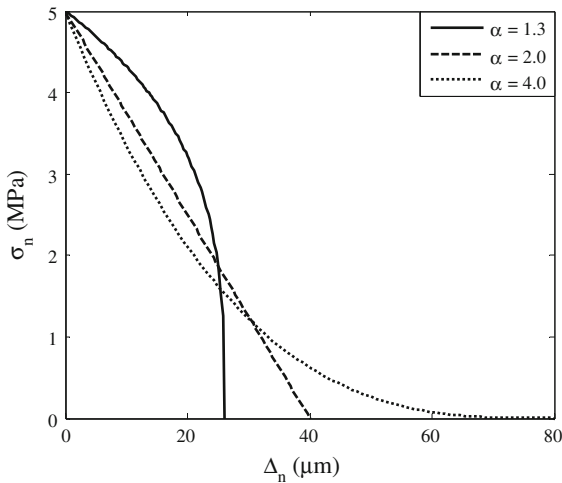
Fig. 4 Illustration of some of the plausible shapes for mode-I extrinsic PPR model for different shape parameters α

that can represent a wide range of softening models previously used in the literature, such as plateau, linear, exponential type, etc simply by changing the shape parameter α, as shown in Fig. 4.

The objective function for the N-M optimization scheme is defined as follows,

$$\min_{\lambda_{coh}} \Phi(\lambda_{coh}) = w_1||\mathbf{F}^{\text{ext}} - \mathbf{F}^{int}||$$
$$+ w_{f1} f_1(\alpha), \qquad \Phi : \mathbb{R}^3 \to \mathbb{R} \quad (10)$$

where, $\mathbf{F}^{int} = (\mathbf{K}_b + \mathbf{K}_{coh}(\boldsymbol{u}, \lambda_{coh})) \, \boldsymbol{u}$; w_1, w_{f1} are the weighting factors. As before, in order to account for the constraints, barrier functions need to be defined. f_1 is the barrier function that ensures $\alpha > 1$.

$$f_1(\alpha) = \sum 10^{\Psi(1-\alpha)} \qquad (11)$$

where, $\Psi >> 1$. Here, as well, the optimization scheme is terminated when the change in objective function is less than 0.1 percent.

4 Numerical examples

In this section, two examples, one for each optimization approach will be shown. Synthetic displacement field data coming from a direct problem solution will be used as the input for the inverse problem. We have also shown that the inverse analysis technique works of any choice of CZM used for the direct problem (Gain 2010) and does not depend on any prior knowledge of the result.

4.1 Problem description

Four point bending of a simply supported single edge notch beam (SENB) undergoing mode-I fracture is used for the illustration. The geometry and boundary conditions are shown in Fig. 1. Plane stress conditions are assumed for the simulations. The bulk material is assumed to be quasi-brittle (i.e., exhibiting linear elastic response everywhere with the exception of the line cohesive zone where all nonlinearities will be concentrated), with Young's modulus $E = 70$ GPa, Poisson's ratio $\nu = 0.25$, and initial crack length a $= 8$ mm. The finite element mesh has finer elements along the axis of symmetry along which the crack will propagate and the elements gradually increase in size towards the supports. The finer elements ensure that the nonlinearity due to the cohesive zone is captured accurately. In order to take advantage of symmetry only half the beam is modeled. The finite element mesh contains 2891 nodes, 2673 Q4 bulk elements and 608 cohesive line elements. Based on a parametric study conducted by Song et al. (2006), the size of the cohesive elements inserted along the line of symmetry is 0.05 mm which is fine enough to capture the nonlinearities due to fracture. In all cases there are at least three elements in the failing cohesive zone. The displacement field of the entire specimen is used as input for the inverse scheme. The software PATRAN is used to generate the meshes, and computational implementation is done in MATLAB.

4.2 Shape optimization approach

As load is applied sequentially in the direct simulation through fixed displacement intervals, the crack at some critical value initiates and then propagates along a straight line resulting in compliance change of the configuration of the beam. The direct problem is solved using 100 displacement controlled loading steps with maximum displacement of 0.13 mm applied in the downward direction. A power law traction-separation is used to spontaneously initiate and grow the crack. The global response in the form of load versus crack mouth opening displacement (CMOD) obtained from the direct simulation is shown in Fig. 5. The software ABAQUS has been used on the same direct problem to verify the results from the numerical implementation developed for this work. As seen in Fig. 5, there is excellent agreement between our MATLAB implementation
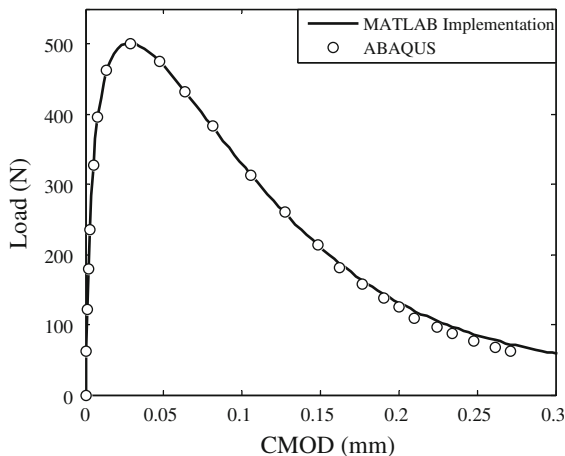
Fig. 5 Load versus CMOD plot for SENB using power relation

and ABAQUS results. All future results of both direct and inverse problems shown in this work will be from our numerical implementation.

A loading step when the crack has propagated significantly into the specimen ligament is selected (specifically, load level = 92 N), and the displacement field corresponding to this loading step is used to run the inverse analysis. Note that the displacement field corresponding to only *one loading step* is used and the selection of the loading step is essentially arbitrary as long as the crack has propagated sufficiently away from the initial pre-crack forming complete cohesive zone. In addition, other than the 2D displacement field at this time instant and the bulk elastic properties, presumably obtained independently, *no other* cohesive parameters are used as input to the optimization scheme. Both cohesive parameters (cohesive strength, cohesive fracture energy) and the shape of the traction-separation relationship are outcomes of the optimization. Figure 6 shows the evolution of the CZM with different iterations of the N-M optimization scheme. The top part of the figure shows the history of the objective function Φ (Eq. 4) during the minimization process. The six panels (*a-f*) below the main figure show the evolution of the traction-separation relation corresponding to the iterations marked in the main figure above. As can be seen neither the maximum cohesive stress, nor the displacement, nor the shape of the curve are predetermined. The relation shown in (*f*), which corresponds to the state after a large number of iterations with near zero Φ, is very similar to that shown in (*e*) illustrating the robust convergence of this scheme after a relatively

small number of iterations. In terms of run time, the 400 iterations correspond to 2–3 min for the current mesh discretization.

In order to verify the inverse analysis implementation, various plausible cases of direct problem conditions have been investigated and the inverse analysis results have been compared to the known direct problem input CZM curves. The process is discussed in the subsequent sections.

4.2.1 Displacement field obtained from various loading steps

One possible source of non-uniqueness of the solution could be the choice of load level from which we pick the displacement field used in the minimization scheme. The implementation needs to be verified for different sets of displacement field data taken from different loading levels to ensure that the extracted CZMs are similar. To this end, displacement fields taken from the direct problem loading levels corresponding to 170, 123, 92, 74 and 56 N, along the descending part of the load-CMOD curve, are used as input and corresponding CZMs extracted from the inverse problem are shown in Fig. 7. Six points are used in the CZM. Based on our numerical experiments, using more than 6 points does not add to the accuracy but rather only adds to the computational cost. The optimization scheme starts with an initial guess for CZM as linear softening between points $(\sigma_n, \Delta_n) = (1, 0)$ and $(0, 0.05)$ and evolves with every iteration, finally converging to the results shown in Fig. 7. As can be seen in Fig. 7, the extracted CZMs are almost identical for the different displacement fields. Thus, as mentioned previously, the displacement field from any loading point can be chosen for the inverse analysis provided that the complete cohesive zone have been formed since crack initiation.

4.2.2 Different number of interpolation points in the CZM

The accuracy of the implementation is tested next when different number of interpolation points ranging from 4 to 7 are used in the CZM. Although interpolation of 7 points can represent most of the CZM available in literature, the implementation is flexible to include as many points as desired. The displacement field from the load level of 92 N is taken with an initial guess of linear softening CZM between the points $(\sigma_n, \Delta_n) = (1, 0)$ and

Fig. 6 Evolution of CZM with different iterations of N-M scheme. Six interpolation points have been used for the CZM evolution. In subplot (*f*), dotted line represents the CZM used for the direct problem
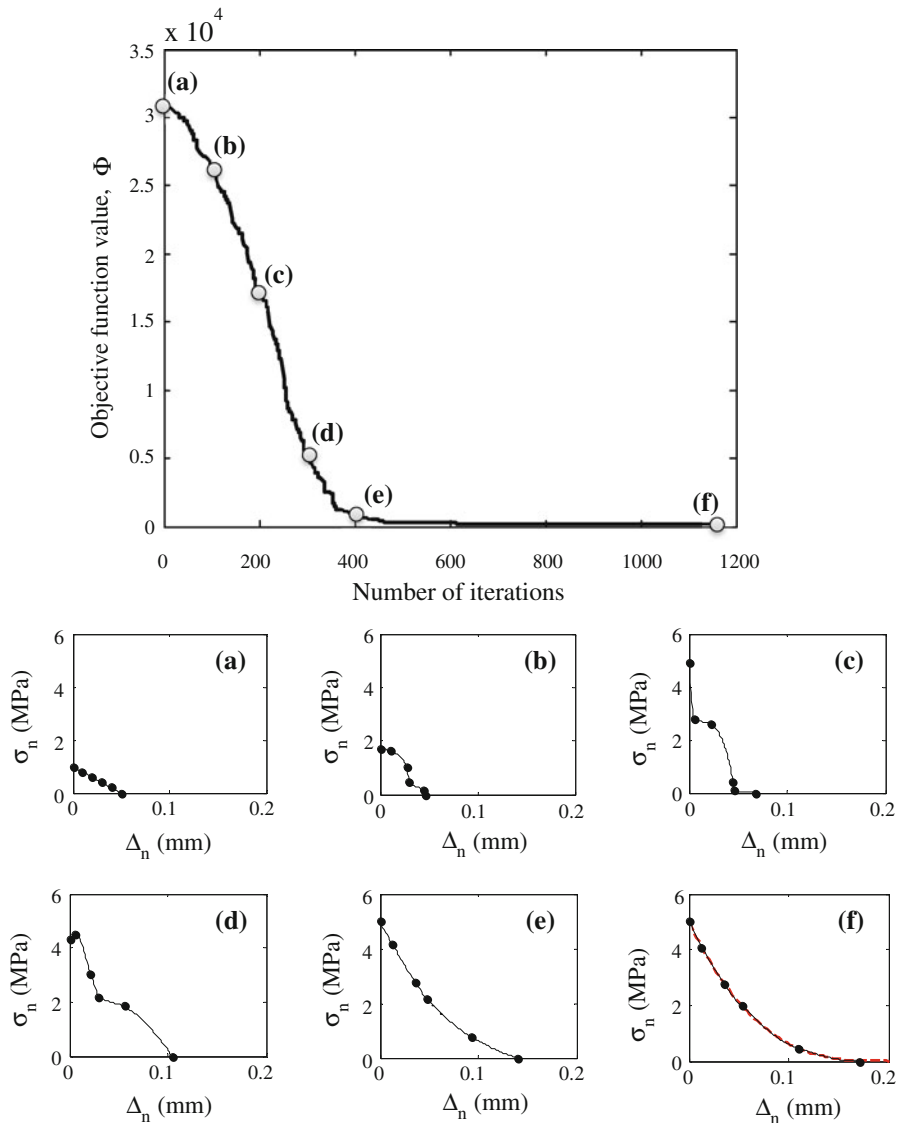
(0, 0.05). Virtually identically shaped CZMs, including the intercept values on the traction and separation axes, are obtained in all the cases as is evident from Fig. 8.

4.2.3 Initial guess for the optimization

Generally the initial guess used in minimization/optimization problems plays a vital role in the converged solutions, especially for highly nonlinear problems. It is important that the algorithm is robust and converges for different initial guesses within reasonable limits. The present numerical implementation has been verified for a large number of different initial guesses

(approximately 50) and the results for two vastly different ones are shown in Fig. 9. Six interpolation points are used to obtain the CZM with the displacement field coming from load level 92 N. Both the over- and the under-estimate converge to almost identical traction-separation relation used in the direct problem.

4.2.4 Noise in the displacement field data

The goal of the current work is to develop a hybrid technique which uses displacement fields obtained from actual experimentation using a technique sensitive to in-plane displacements, such as digital image
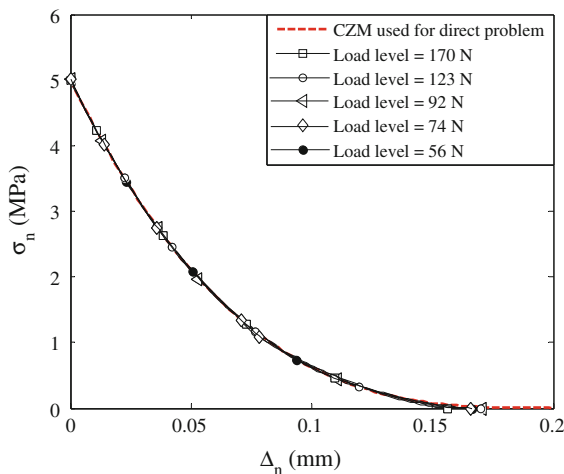
Fig. 7 Extracted CZMs using displacement fields from various loading points in direct problem. Six interpolation points have been used for the CZM evolution
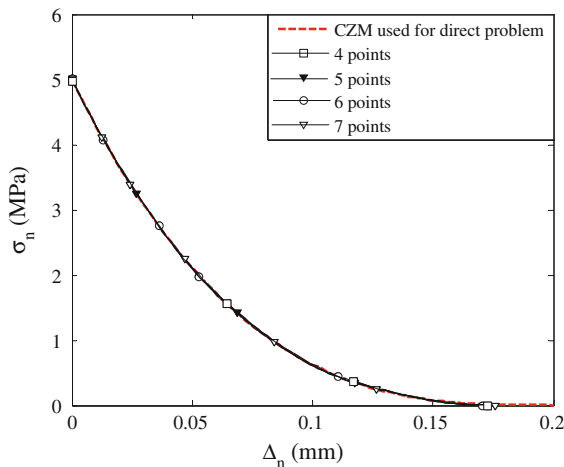

Fig. 8 Extracted CZMs using different number of interpolation points in the numerical scheme. Displacement field at 92 N load has been used
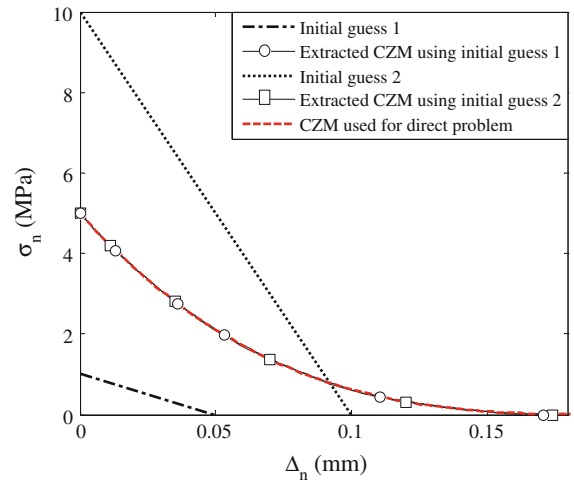

Fig. 9 Extracted CZMs for different initial guesses

Table 1 Levels of noise added to synthetic displacement field data obtained from the direct problem

Maximum noise (μm)	Standard deviation in noise (μm)	Percentage noise
0	0	0
0.1	0.05–0.07	0.02
1.0	0.35–0.55	0.20
10.0	3.47–4.92	2.00

of 0.005 pixels or higher (Lu and Cary 2000; Shen 2009). Overall, this technique can resolve quantities of the order of 0.0005–0.5 μm or better. The levels of noise that have been analyzed in this work are shown in Table 1. Noise added to the synthetically obtained displacement field data from the direct problem solution is randomly generated from a standard uniform distribution on the open interval (0,1). Percentage noise refers to the average of the percentage deviations of the nodal noisy displacement values from the corresponding nodal synthetic displacement values, over all the nodes.

Percentage noise

$$= \sum_{i=1}^{Total\ nodes} \left(\left| \frac{u_i^{noisy} - u_i^{synthetic}}{u_i^{synthetic}} \right| \times 100 \right)$$

Six interpolation points are used in the CZM. Displacement fields are taken from load level of 92 N. Results using the noisy data are close to the case with no noise in data (Fig. 10)
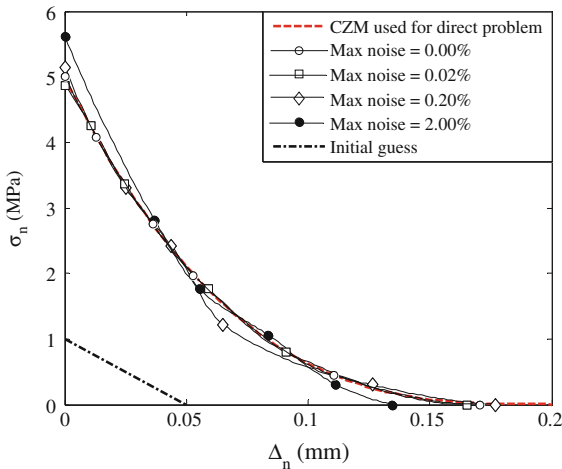
correlation (DIC) (see Sect. 5.1). Unlike the results of the direct numerical simulation used above, DIC, as any other experimental technique, will have noise embedded in its results. So it is vital that the inverse code be able to robustly handle noise in the input displacement field data. The primary source of noise in DIC measured displacements can be related to (1) the resolution of the digital camera being used for DIC, and (2) the details of the DIC correlation algorithm employed. Modern cameras and optics can achieve resolutions up to the order of 0.1–100 μm/pixel or better. Correlation algorithms are known to obtain a sub-pixel accuracy

Fig. 10 Extracted CZMs using displacement field with various levels of noise

Fig. 11 Load versus CMOD plot from implementation for SENB using extrinsic PPR with shape parameter $\alpha = 1.3$

4.3 Parameter optimization for the PPR potential-based CZM

In this section, numerical examples for parameter optimization for the PPR potential-based CZM technique are demonstrated. Displacement fields needed for inverse analysis are again obtained synthetically from the direct problem. The cohesive zone model used is generated from the PPR model with a shape parameter $\alpha = 1.3$, fracture energy $\phi_n = 500$ N/m and cohesive strength $\sigma_n = 5$ MPa. The direct problem is solved using 100 intervals of displacement controlled loading. The global response in the form of load versus CMOD is shown in Fig. 11 for this case. As can be seen, it is different in nature than that shown in Fig. 5, with the longer saturation load duration being a direct result of the PPR model used.

In the parameter optimization for the PPR potential-based CZM approach, the cohesive parameters that are being optimized are $\lambda_{coh} = \{\phi_n, \sigma_n, \alpha\}$ contrary to the previous scheme where the cohesive parameters were the coordinates of the interpolation points. The idea here is to optimize the cohesive parameters and substitute back into the closed form equation of PPR to get the CZM associated with material fracture. A load level of 286 N is picked for the displacement field. Six interpolation points are used in the CZM with an initial guess for CZM as linear softening between points $(\sigma_n, \Delta_n) = (1, 0)$ and $(0, 0.05)$. Inverse analysis is carried out using the displacement field resulting from the direct
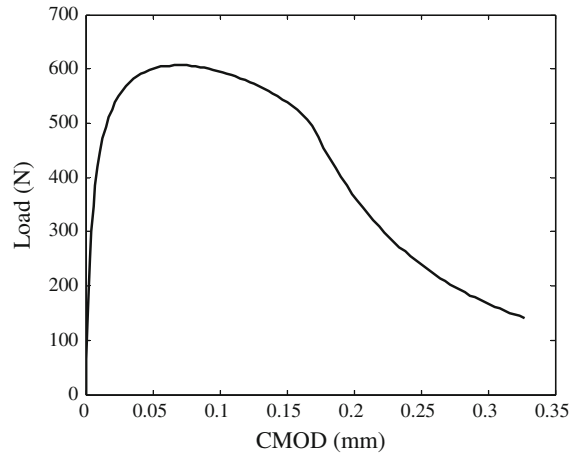
problem. The evolution of CZM with different iterations of the N-M optimization scheme is shown in Fig. 12.

4.3.1 Displacement field obtained from different loading steps

We again verify the parameter optimization for the PPR model approach implementation for different sets of displacement field data. Displacement fields from loading levels 533, 399, 217 and 170 N on the descending branch of the load versus CMOD curve are considered, and corresponding extracted CZMs are shown in Fig. 13. The optimization scheme starts with an initial guess for CZM as linear softening between points $(\sigma_n, \Delta_n) = (1, 0)$ and $(0, 0.05)$. The CZM evolves with each iteration, finally converging to the results shown in Fig. 13. The extracted CZMs are virtually identical for different displacement fields.

4.3.2 Initial guess for the optimization

The implementation is next verified for different initial guesses (approximately 50) and the results for two of them are shown in Fig. 14. The displacement field from load level 286 N is taken.

4.3.3 Noise in the displacement field data

Different levels of noise in the displacement field data are again considered to demonstrate the robustness of

Fig. 12 Evolution of CZM with different iterations of N-M scheme. In subplot (f), dotted line represents the CZM used for the direct problem
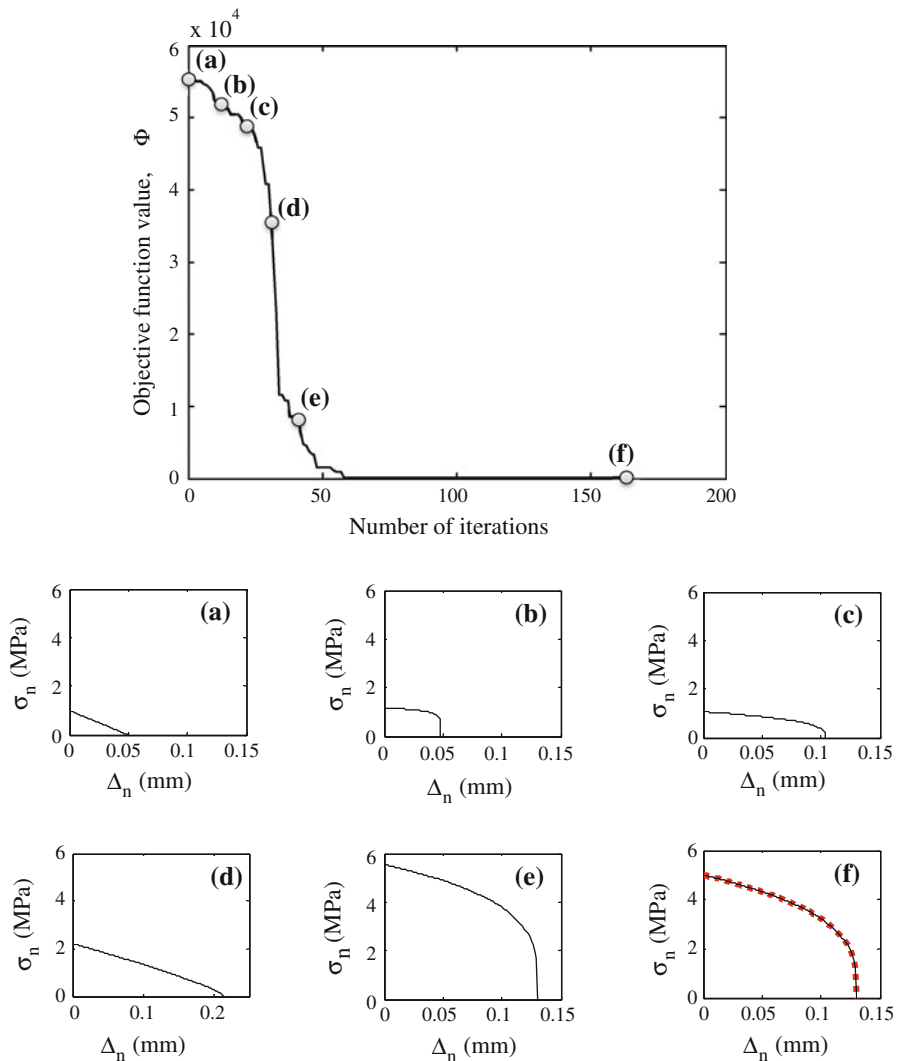
the proposed scheme. Figure 15 shows plots of the extracted CZM using displacement field data with the levels of noise shown in Table 1. The results using noisy displacement field data are similar to the case with no noise in the data.

5 Validation experiments using PMMA

The technique is applied to Polymethyl Methacrylate (PMMA), modeled as a quasi-brittle material where all non-linearity is concentrated in a line cohesive zone ahead of the crack tip. The section starts with the description of experimental setup for a four point bending experiment of PMMA and, the corresponding DIC experimental results. Thereafter, computational results

are shown using both the shape optimization approach and the parameter optimization for the PPR potential-based CZM.

5.1 Experimental setup and DIC experiments

PMMA is chosen because at the rates and temperatures used in this work, it exhibits only limited plasticity and generally fails in a brittle fashion through crazing (Li and Lambros 2001; Morgan and Ward 1977). Specimens were machined to the dimensions shown in the photograph of Fig. 16. The PMMA chosen for the experiment had a Young's modulus of 3.25 GPa and Poisson's ratio 0.35. Prior to testing, the following
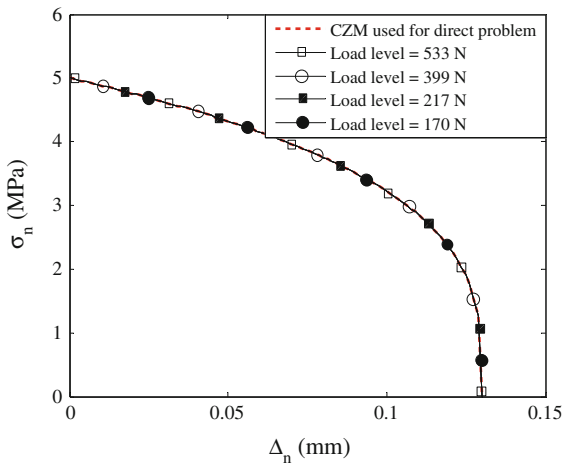
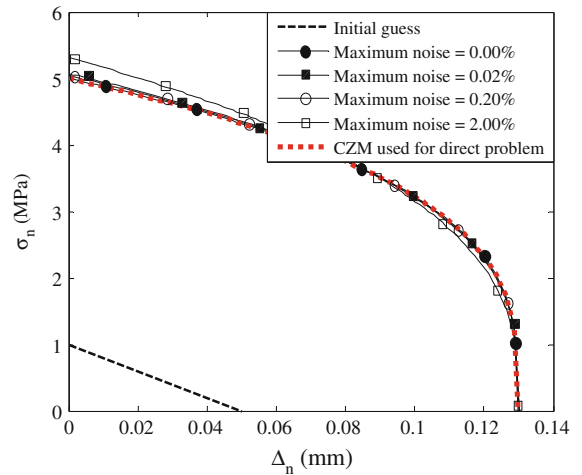**Fig. 13** Extracted CZMs using displacement fields from different loading points in direct problem
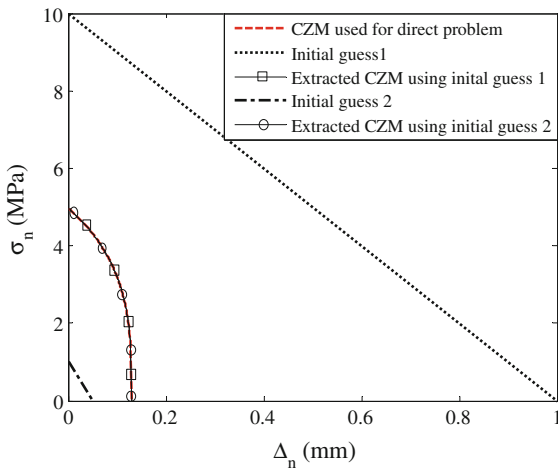
Fig. 14 Extracted PPR CZMs for different initial guesses

Fig. 15 Extracted CZMs using displacement field with various levels of noise

procedure was employed to create a sharp crack—a prerequisite for valid material failure property measurements. First, a 15 mm long and 1 mm wide notch was cut with a bandsaw. A razor blade was then used to extend the notch by 3 mm in what was a sharper, crack-like feature, but still not a sharp crack. The specimen was then placed in a servohydraulic load frame in the four point bend configuration shown in Fig. 16. The top of the specimen was supported by two semicircular cylinders spaced 80 mm apart while the bottom was loaded by two semicircular cylinders spaced 280 mm apart. To create a microstructurally sharp crack, the specimen was then fatigue loaded in four point bending to grow a crack from the razor notch to a total length of 35.5 mm.

Load control was used for this fatigue loading; consequently, the stress intensity factor amplitude ΔK, increased with the crack length. To keep a relatively constant ΔK level throughout fatigue crack growth, the load was dropped periodically so that ΔK was always between 1.45 and 1.60 MPa$\sqrt{\text{m}}$. The loading frequency was 2 Hz with a loading ratio, R, (minimum load divided by maximum load) of 0.05. Approximate crack length was determined by markings drawn on the specimen before it was placed in the load frame. Eventually, digital images at a known scale were used for much higher accuracy measurements of the final crack length. Fatigue loading was stopped once the total crack length reached 35.5 mm ($a/W = 0.29$). The specimen was then loaded monotonically to failure in the manner described later, during which time the displacement field measurements were made.

We obtained full-field displacement measurements using the non-contact optical technique of Digital Image Correlation (DIC). Speckled patterned images recorded before and after the deformation are correlated to obtain the displacement and strain fields. The ability of DIC to provide full field displacement field, which is precisely the input needed in our minimization scheme, was the main motivation behind using DIC in the current work.

A speckle pattern was applied to the front of the specimen using black and white spray paint. An IMI-Tech model IMB-202FT firewire camera with a resolution of 1,600× 1,200 pixels was used to capture images
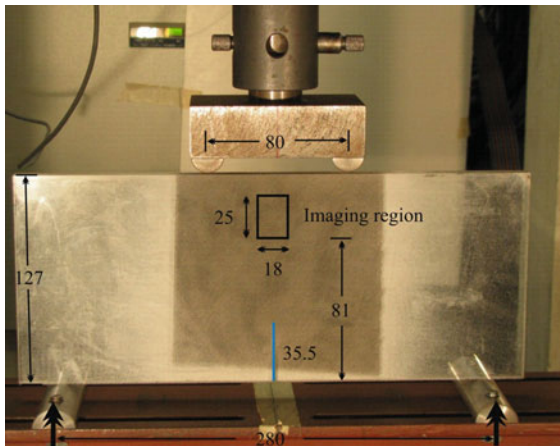
Fig. 16 Specimen dimensions and loading configuration for both fatigue cracking and monotonic loading (dimensions in mm)

Fig. 17 Load-displacement measurement during monotonic loading phase. Each point on the plot represents the time at which an image was captured. The images used for DIC results shown in this paper are indicated by arrows

throughout the experiment at a rate of 7.5 frames per second and a scale of 15.3. Lighting was provided by two 250 W halogen lights aimed at the specimen. A Labview program, developed by National Instruments Corporation, was used to control both the load frame and the camera, allowing for precise synchronization of captured images with load levels—an important feature for relating the experimental measurements to corresponding load levels from the simulations. The specimen was loaded in displacement control at a constant rate of 0.02 mm/s. During the monotonic loading experiment, a crack initiated from the fatigue crack and grew in a stable manner across the entire specimen width. Images were captured within the rectangular region outlined in Fig. 16 during both the pre-initiation phase and the crack growth phase of monotonic loading. At the same time, far-field applied load was recorded by a load cell. Figure 17 shows the load versus load line displacement measurement during the monotonic loading phase. While load and displacement measurements were taken every 10 ms, Fig. 17 shows only those data points corresponding to times at which images were acquired.

Digital image correlation was performed on images captured throughout the experiment in order to obtain displacement measurements for the cohesive models. The DIC reference image was captured before monotonic loading began with a preload force of 0.1 kN on the specimen. Of primary interest are the images in which the crack was propagating through the imaging region. The DIC results used for this work are from
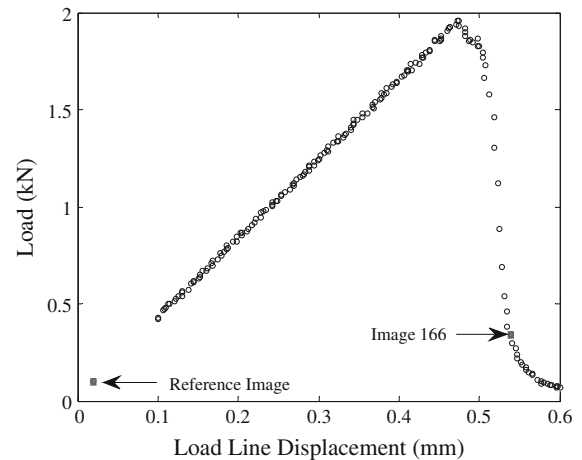
image number 166, indicated in Fig. 17, in which the crack had grown through the majority of the imaging region. Correlation was performed using commercially available digital image correlation software (Vic2d developed by Correlated Solutions Inc.) with a subset size of 101 by 101 pixels, a subset spacing of 15 pixels, and second order displacement gradients. Figure 18 shows the DIC displacement fields u and v (perpendicular and parallel to the crack respectively) corresponding to the applied displacement level of 0.55 mm (image 166), i.e., well after the crack has initiated. The displacement fields shown in Fig. 18 have been modified from the raw DIC results to relate them to the cohesive models. Note that only a subset of the entire specimen need have the displacement field specified. Since the cohesive models assume symmetry about the crack line, only half of the DIC displacement field was used. Rigid translation was estimated and subtracted from the displacement fields, but rigid rotations (around $0.05°$) and mode-II crack opening effects were not subtracted from the displacement field as they were found to be negligible based on the authors' analysis. DIC displacement fields are less reliable when spanning the discontinuity across the crack plane, and the fracture process zone. We therefore eliminate a region approximately 1 mm (0.008 H) next to the crack plane. For the inverse analysis, we consider displacement fields approximately up to a distance of 0.05 H

Fig. 18 Segment of DIC displacement fields for the right half of image number 166. **a** Contour plot of v-displacements (*parallel to the crack line*). **b** Contour plot of u-displacements (*perpendicular to the crack line*). In these plots, the origin for these plots is on the crack line at the notch mouth
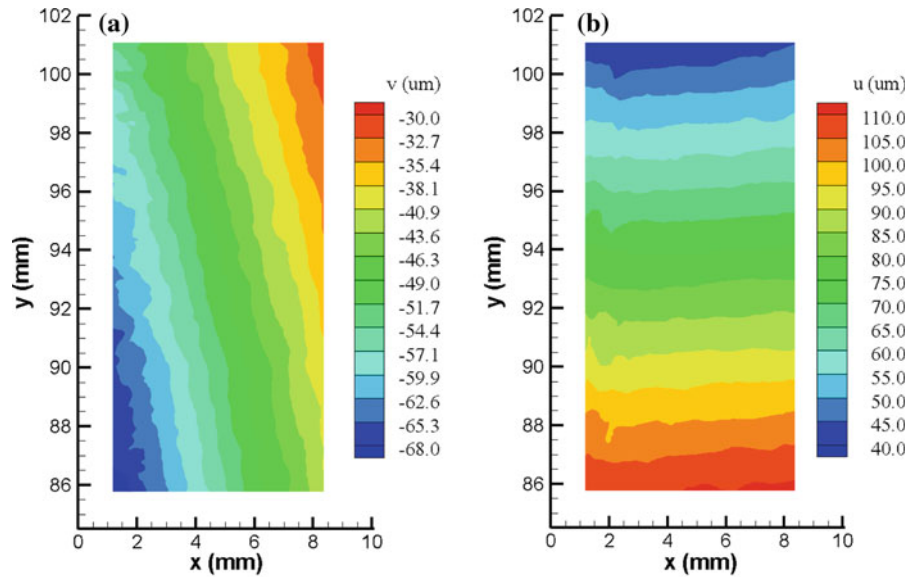
(6 mm) horizontally from the crack plane and 0.15 H (19 mm) vertically downwards from the crack tip.

5.2 Results from inverse analysis

The geometry of the specimen that was modeled numerically is that shown in Fig. 16. In order to take advantage of symmetry only half of the beam is simulated. The finite element mesh used for this inverse analysis is shown in Fig. 19.

The initial guess for the inverse analysis is taken as a linear softening curve between the points $(\sigma_n, \Delta_n) = (1, 0)$ and $(0, 0.05)$.

5.2.1 Shape optimization approach

The inverse analysis was performed initially with six interpolation points for the CZM traction-separation relation. Piecewise cubic Hermite interpolation is used to interpolated between the optimized points to obtain a complete curve. Even with the robustness studies done before, the actual error is significant enough to necessitate smoothing the DIC displacements to acceptable noise levels. Different levels of displacement field data smoothing was tried. The extracted CZMs are shown in Fig. 20, where p refers to the level of smoothing applied to experimental displacement field data (p = 0, represents a least square straight line fit to the data and

p = 1 represents a cubic spline interpolation). Smoothing of the experimental displacement field data is performed using MATLAB function *csaps,* which returns a smoothing spline function f, which minimizes the objective,

$$H = p \sum_{j=1}^{n} w(j)|y(:, j) - f(x(j))|^2 (1 - p) \int \tau(t)|D^2 f(t)^2 dt$$

where, w is the weight vector; $x(j)$ is the data site with data value $y(:, j)$; τ is the piecewise constant weight function; $D^2 f$ denotes the second derivative of function f and n is the number of entries of x.

The shapes of the CZMs show a similar trend with cohesive strength of around 35 MPa and critical crack opening of 30 , both reasonable quantities for PMMA. For PMMA, Elices (2002) reported a cohesive strength of 80 MPa and a critical crack opening of 3.8 µm. Murphy et al. (2006) obtained a cohesive strength of 80 MPa and a critical crack opening of 2.1 µm. After trying different levels of smoothing, CZMs whose shapes are similar to ones available in literature (Elices 2002; Murphy et al. 2006), are obtained corresponding to smoothing parameter p in the range of 0.6–0.8 (Fig. 20). From the set of CZMs obtained above, the CZM with p = 0.6 is assumed as the representative CZM (since the shape of this CZM is closest to the shape of the CZM used by Elices 2002), and will be used here

Fig. 19 Finite element discretization for PMMA specimen **a** Left portion of the specimen, **b** Meshing detail
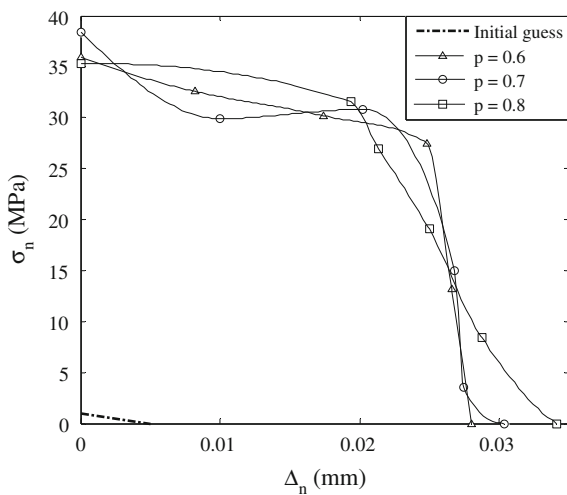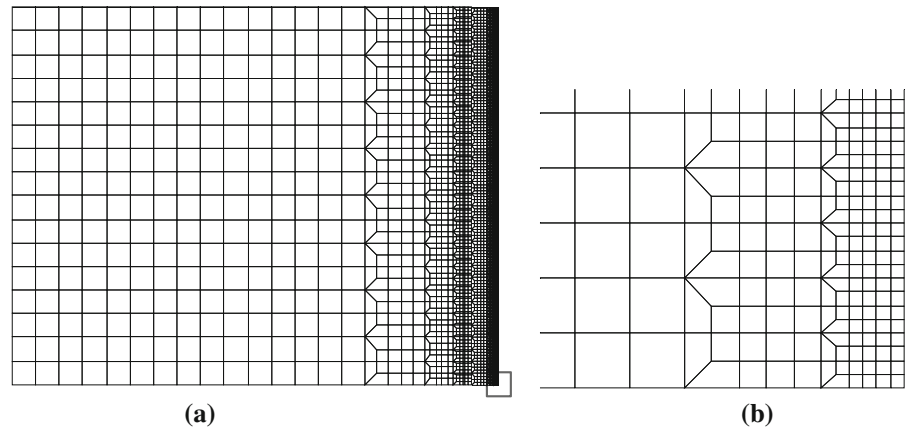

(a)   **(b)**

Fig. 20 Extracted CZMs using shape optimization technique for different levels of displacement field smoothing

Fig. 21 Comparison between the experimental and simulation global responses of PMMA specimen

onwards for discussions pertaining to the shape optimization approach.

As an additional verification, the direct problem is solved using the representative CZM ($p = 0.6$) obtained from the inverse problem. The load versus load line displacement (LLD) plot from the experiments (Fig. 17) and the direct problem simulations are shown in Fig. 21. Both results are close to each other which gives confidence in the extracted CZM. The peak strength is not captured as accurately, possibly because the displacement fields are not being resolved accurately enough or the cohesive zone length is very small for PMMA (of the order of microns) which is difficult to resolve using inverse analysis. Our simulations showed cohesive zone lengths of 20–200 µm. Note that further mesh
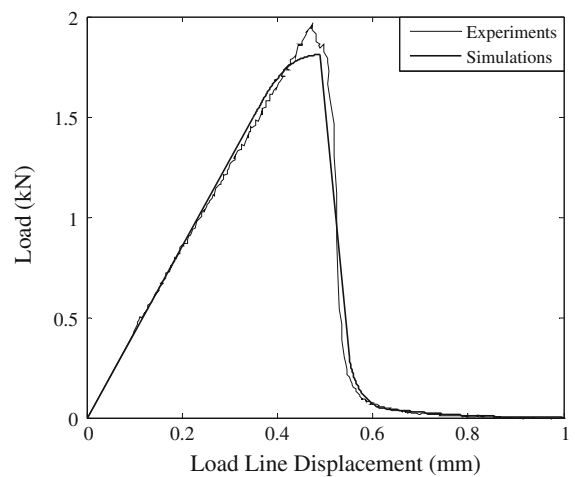
refinement may provide more accurate results, but only if the DIC results were comparably refined also. (Otherwise we would be merely generating extrapolated data for assignment to the finer FEA mesh.) Furthermore, it should be noted that there is an obvious tradeoff between the refinement level used and the computational cost associated with it.

The extracted CZM can also be verified by comparing fracture energies. For the experiments, the fracture energy is taken as the area under the load versus LLD curve divided by fracture area, calculated at 0.75 N/mm. For the simulations, the fracture energy is computed as,

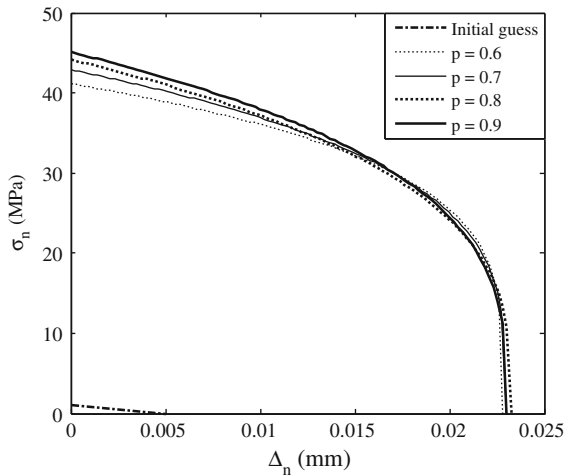$$G = \int_{0}^{\Delta_c} \sigma_n \cdot d\Delta_n \tag{12}$$

Fig. 22 Extracted CZMs using PPR model for different levels of displacement field smoothing

Fig. 23 Comparison between the experimental and simulation global responses of PMMA specimen

which yielded approximately 0.61 N/mm for the representative CZM used. Overall the simulations resulted in fracture energy in the range of 0.61 ± 0.35 N/mm for all the CZMs in the solution set.

5.2.2 Parameter optimization for the PPR potential-based CZM

Results for the inverse analysis of PMMA using the parameter optimization for the PPR potential-based CZM technique will be shown next. The initial guess is the same as the shape optimization case which corresponds to PPR model parameters $(\lambda_{coh})_{initial} = \{\phi_n = 2.5\,\text{N/m}, \sigma_n = 1.0\,\text{MPa}, \alpha = 2\}$ The extracted CZMs are shown in Fig. 22. As before, parameter p refers to the level of smoothing applied to the experimental data. The shapes of the CZMs, using the PPR model, show a similar trend with an average cohesive strength of around 42 MPa and critical crack opening of 23 μm. From the set of CZMs obtained above, the CZM with p = 0.6 is assumed as the representative CZM (to be consistent with the smoothing to the displacement field data in Sect. 5.2.1), and will be used here onwards for discussions pertaining to parameter optimization for the PPR potential-based CZM approach.

The direct problem is again solved using the representative CZM from the PPR parameters minimization. The load versus load line displacement (LLD) plot from the experiments and simulations are shown in Fig. 23 where a similar agreement to that seen earlier (Fig. 21)
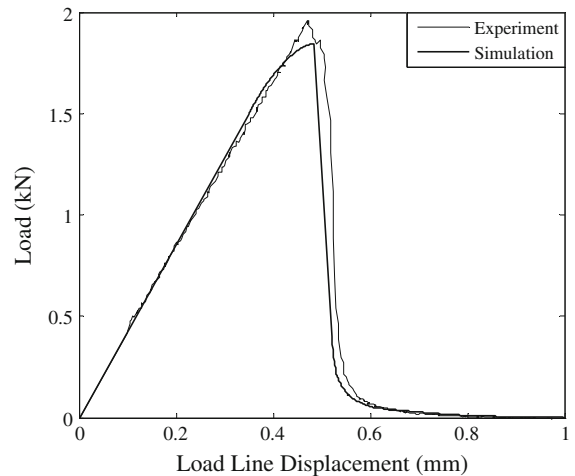
is observed. However, once again the peak load is also not captured accurately.

The fracture energy directly obtained directly through parameter optimization for the PPR potential-based CZM is approximately in the range $0.68 \pm 0.15\,\text{N/mm}$ for all the CZMs in the solution set, as compared with the 0.75 N/mm experimental value.

6 Conclusions

A hybrid experimental/numerical technique to acquire cohesive fracture properties of a quasi-brittle material for mode-I fracture has been proposed. The technique involves a computational scheme of inverse analysis and optical experimentation based on DIC. Two approaches for the inverse analysis have been suggested, namely: a shape optimization approach and a parameter optimization for the PPR potential-based CZM. The shape optimization approach and parameter optimization for the PPR potential-based CZM, have been verified for a power relation CZM and a plateau type CZM (shape parameter $\alpha = 1.3$) respectively. The approaches have proven to be robust for various cases of different initial guesses, various synthetic and noisy displacement field data. As a proof of concept, the proposed techniques have been applied to a PMMA quasi-static crack growth experiment. The shape of the CZM, cohesive strength, and fracture energy obtained for PMMA through both the techniques are very comparable to each other, and to the ones available in the

literature. For final verification of the extracted CZM, the global response in the form of load versus LLD and the fracture energy were compared to those measured experimentally. The results were in good agreement. Improved results can be obtained by employing higher resolution DIC imaging and finer meshes for the inverse analysis.

References

Abanto-Bueno J, Lambros J (2005) Experimental determination of cohesive failure properties of a photodegradable copolymer. Exp Mech 45(2):144–152

Alfano G (2006) On the influence of the shape of interface law on the application of cohesive-zone models. Compos Sci Technol 66:723–730

Andersson T, Stigh U (2004) The stress-elongation relation for an adhesive layer loaded in peel using equilibrium of energetic forces. Int J Solids Struct 41:413–434

Avril S, Bonnet M, Bretelle AS, Grediac M, Hild F, Ienny P, Latourte F, Lemosse D, Pagano S, Pagnacco E, Pierron F (2008) Overview of identification methods of mechanical parameters based on full-field measurements. Exp Mech 48:381–402

Barenblatt GI (1959) The formulation of equilibrium cracks during brittle fracture: general ideas and hypothesis, axially symmetric cracks. PMM 23:434–444

Budiansky B, Evans AG, Hutchison JW (1995) Fiber-matrix debonding effects on cracking in aligned fiber ceramic composites. Int J Solids Struct 32:315–328

Calderon AP (1980) On an inverse boundary value problem. In: Seminar on numerical analysis and its applications to continuum physics. Soc. Brasilian de Matematica, Rio de Janeiro, pp 65–73

Camacho GT, Ortiz M (1996) Computational modeling of impact damage in brittle materials. Int J Solids Struct 33:2899–2938

Chandra N, Li H, Shet C, Ghonem H (2002) Some issues in the application of cohesive zone models for metal-ceramic interfaces. Int J Solids Struct 39:2827–2855

Claire D, Hild F, Roux S (2004) A finite element formulation to identify damage fields. Int J Numer Methods Eng 61:189–208

Cottin N, Felgenhauer HP, Natke HG (1984) On the parameter identification of elastomechanical systems using input and ouput residuals. Ing Arch 54:378–387

Dugdale DS (1960) Yielding of steel sheets containing cracks. J Mech Phys Solids 8:100–104

Elices M (2002) The cohesive zone model: advantages, limitations, and challenges. Eng Fract Mech 69:137–163

Gain AL (2010) A hybrid technique to extract cohesive fracture properties of elasto-plastic materials using inverse analysis and digital image correlation. M.S. Thesis. University of Illinois at Urbana-Champaign

Geubelle PH, Baylor J (1998) Impact induced delamination of laminated composites: a 2D simulation. Compos Part B Eng 29:589–603

Grédiac M, Pierron F (2006) Applying the virtual fields method to the identification of elasto-plastic constitutive parameters. Int J Plast 22:602–627

Gu P (1995) Notch sensitivity of fiber-reinforced ceramics. Int J Fract 70:253–266

Hillerborg A, Modeer M, Petersson PE (1976) Analysis of crack formation and crack growth in concrete by means of fracture mechanics and finite elements. Cement Concr Res 6:773–782

Kandula SSV, Abanto-Bueno J, Geubelle PH, Lambros J (2006) Cohesive modeling of quasi-static fracture in functionally graded materials. J Appl Mech 73(5):783–791

Kaute DAW, Shercliff HR, Ashby MF (1993) Delamination, fibre bridging and toughness of ceramic matrix composites. Acta Metall Mater 41(7):1959–1970

Knauss WG, Chasiotis I, Huang Y (2003) Mechanical measurements at the micro and nanometer scales. Mech Mater 35:217–231

Ladevèze P, Nedjar B, Reynier M (1994) Updating of finite element models using vibration tests. AIAA 32:1485–1491

Li Z, Lambros J (2001) Strain rate effects on the thermomechanical behavior of polymers. Int J Solids Struct 38:3549–3562

Lu H, Cary PD (2000) Deformation measurements by digital image correlation: implementation of a second-order displacement gradient. Exp Mech 40:393–400

McNeill SR, Peters WH, Sutton MA (1987) Estimation of stress intensity factor by digital image correlation. Eng Fract Mech 28:101–112

Morgan GP, Ward IM (1977) Temperature dependence of craze shape and fracture in polymethyl methacrylate. Polymer 18:87–91

Murphy N, Ali M, Ivankovic A (2006) Dynamic crack bifurcation in PMMA. Eng Fract Mech 73:2569–2587

Needleman A (1987) A continuum model for void nucleation by inclusion debonding. J Appl Mech 54:525–531

Nelder JA, Mead R (1965) A simplex method for function minimization. Comput J 7:308–313

Nocedal J, Wright SJ (2006) Numerical optimization. Springer, Berlin

Pagnacco E, Lemosse D, Hild F, Amiot F (2005) Inverse strategy from displacement field measurement and distributed forces using FEA. In: 2005 SEM annual conference and exposition on experimental and applied mechanics, Portland, 7–9 June 2005

Park K (2005) Concrete fracture mechanics and size effect using a specialized cohesive zone model. MS Thesis. University of Illinois at Urbana-Champaign

Park K, Paulino GH, Roesler JR (2009) A unified potential-based cohesive model of mixed-mode fracture. J Mech Phy Solids 57:891–908

Peters WH, Ranson WF (1982) Digital imaging techniques in experimental stress analysis. Opt Eng 21:427–431

Peters WH, Ranson WF, Sutton MA, Chu TC, Anderson J (1983) Application of digital image correlation methods to rigid body mechanics. Opt Eng 22:738–742

Ritchie RO (1997) On growth of fatigue cracks in advanced ceramics and intermetallics. Advances in Fracture Research. Proceedings of the Ninth International Conference on Fracture, Sydney, Australia 3:1211

Ritchie RO, Cannon RM, McNaney JM (1997) Interfacial and near-interfacial fracture in ceramics/metal layered systems. Advances in fracture research. In: Proceedings of the ninth international conference on fracture. Sydney, Australia 6:3119

Shen B (2009) Functionally graded fiber—reinforced cementitious composites : manufacturing and extraction of cohesive properties using finite elements and digital image correlation. PhD Thesis. University of Illinois at Urbana-Champaign

Shen B, Paulino GH (2010a) Direct extraction of cohesive fracture properties from digital image correlation: A hybrid inverse technique. Exp Mech. doi:10.1007/s11340-010-9342-6

Shen B, Stanciulescu I, Paulino GH (2010b) Inverse computation of cohesive fracture properties from displacement fields. Inverse Probl Sci Eng. Accepted

Song SH (2006) Fracture of asphalt concrete: A cohesive zone modeling approach considering viscoelastic effects. PhD Thesis. University of Illinois at Urbana-Champaign

Song SH, Paulino GH, Buttlar WG (2006) Simulation of crack propagation in asphalt concrete using a cohesive zone model. J Eng Mech 132(11):1215–1223

Song SH, Paulino GH, Buttlar WG (2008) Influence of cohesive zone model shape parameter on asphalt concrete fracture behavior. AIP Conf Proc 973:730–735

Sorensen BF, Jacobsen TK (1998) Large-scale bridging in composites: R-curves and bridging laws. Compos Part A 29:1443–1451

Spearing SM, Evans AG (1992) The role of fiber bridging in the delamination resistance of fiber-reinforced composites. Acta Metall Mater 40:2191–2199

Sutton MA, Wolters WJ, Peters WH, Ranson WF, Mcneil SR (1983) Determination of displacements using an improved digital image correlation method. Image Vis Comput 1:133–139

van Mier JGM, van Vliet MRA (2001) Uniaxial tension test for the determination of fracture parameters of concrete: state of the art. Eng Fract Mech 69:235–247

Volokh KY (2004) Comparison between cohesive zone models. Commun Numer Methods Eng 20:845–856

Xu X, Needleman A (1993) Void nucleation by inclusion debonding in a crystal matrix. Model Simul Mater Sci Eng 1:111–132